Talanta 273 (2024) 125959

Contents lists available at ScienceDirect

Talanta

journal homepage: www.elsevier.com/locate/talanta

Confinement-enhanced electrochemiluminescence by Ru(dcbpy)$_3^{2+}$-functionalized γ-CD-MOF@COF-LZU1 porous hybrid material as micro-reactor for CYFRA 21-1 detection

Xiang Ren [a], Mingyue Shao [a], Xiaofei Li [a], Zuoxun Xie [a], Jinxiu Zhao [a,b], Huan Wang [a], Min Gao [a,d,**], Dan Wu [a,*], Huangxian Ju [a,e], Qin Wei [a,c,***]

[a] Key Laboratory of Chemical Sensing & Analysis in Universities of Shandong, School of Chemistry and Chemical Engineering, University of Jinan, Jinan 250022, China
[b] School of Materials Science and Engineering, University of Jinan, Jinan 250022, China
[c] Department of Chemistry, Sungkyunkwan University, Suwon, 16419, Republic of Korea
[d] State Key Laboratory of Biobased Material and Green Papermaking, Qilu University of Technology (Shandong Academy of Sciences), Daxue Rd, Changqing District, Jinan, Shandong 250353, China
[e] State Key Laboratory of Analytical Chemistry for Life Science, School of Chemistry and Chemical Engineering, Nanjing University, Nanjing 210023, China

ARTICLE INFO

Keywords:
Electrochemiluminescence
Ru(dcbpy)$_3^{2+}$
Noble metal aerogels
Synergistic effects
CYFRA 21-1

ABSTRACT

The improvement of electrochemiluminescence (ECL) performance relies on the electron transfer efficiency between luminophore and coreactant. An ultrasensitive ECL micro-reactor with confinement-enhanced performance was prepared by using the covalent organic framework-LZU1-functionalized metal-organic framework (MOF@COF-LZU1) as a platform to assemble enormous *N,N*-dibutyl-2-hydroxyethylamine (DBAE) and tris(4,4′-dicarboxylic acid-2,2′-bipyridyl) ruthenium(II) [Ru(dcbpy)$_3^{2+}$] into its pore channels. Compared to individual substances of γ-CD-MOF and COF-LZU1, the synergistic effects can conduce to the enhancement of the intensity, durability and sensitivity of the micro-reactor. Besides, COF-LZU1 can provide a mild environment to accommodate a certain amount of DBAE by concentrating them from the aqueous solution into its hydrophobic cavities and boost the oxidation efficiency of DBAE to generate more DBAE$^{\bullet+}$ and profited the survival of DBAE$^{\bullet}$, leading to an improved reaction efficiency with the Ru(dcbpy)$_3^{2+}$ intermediate. Thanks to the confinement-enhanced strategy, engineered as high-functioning luminescent materials, Ru@γ-CD-MOF@COF-LZU1 micro-reactors decorated with Au NPs can facilitate electron transfer and capture primary antibodies (Ab_1). Moreover, Au–Pd–Pt noble metal aerogels (NMAs) functionalized MoS_2 NFs (Au–Pd–Pt NMAs@MoS_2 NFs) were chosen as base material due to its large specific surface areas, high porosity, and excellent electrical conductivity. Based on above merits, the sensor demonstrated a sensitive response to CYFRA 21-1 detection in a linear concentration gradient from 10 fg/mL to 50 ng/mL with a detection limit of 0.0055 pg/mL (S/N = 3). The COF-LZU1 decorated ECL micro-reactors were constructed based on the signal amplification strategies to realize accurate CYFRA 21-1 detection.

1. Introduction

On account of the easy miniaturization [1], favorable controllability [2] and strong specificity [3], electrochemiluminescence (ECL) as a detection means have sparked widespread concerns in various areas involving immunoassays [4], aptasensors [5] and environmental detection [6]. Tris-bipyridine ruthenium (Ru(bpy)$_3^{2+}$) and its derivatives are classical ECL reagents [7], which have been widely investigated within the scope of bioanalytical, environmental test and food analysis. In this luminescence system (Ru(bpy)$_3^{2+}$/TPrA), ECL emission markedly

* Corresponding author.
** Corresponding author. Key Laboratory of Chemical Sensing & Analysis in Universities of Shandong, School of Chemistry and Chemical Engineering, University of Jinan, Jinan 250022, China.
*** Corresponding author. Key Laboratory of Chemical Sensing & Analysis in Universities of Shandong, School of Chemistry and Chemical Engineering, University of Jinan, Jinan 250022, China.
E-mail addresses: shdgaomin@whu.edu.cn (M. Gao), wudan791108@163.com (D. Wu), sdjndxwq@163.com (Q. Wei).

https://doi.org/10.1016/j.talanta.2024.125959
Received 3 February 2024; Received in revised form 1 March 2024; Accepted 19 March 2024

boosts with the assistance of TPrA. In this analysis method, numerous ECL sensors have been established based on the signal amplification strategies. The general strategies are introduced nanomaterials with good performance as a platform to load numerous luminophore molecules and promote the redox processes to enhance the ECL efficiency in this work. For the former, C_3N_4 nanosheets (NSs) [8], SiO_2-nanomembrane [9], metal-organic frameworks (MOFs) and covalent organic frameworks (COFs) are most commonly used nanomaterials to cooperate on facilitating ECL emission [10,11]. For the latter, shortening the electron transfer path by covalently linking the co-reactant to the luminophore in a system is an effective way to promote ECL emission. However, whether it is the introduction of nanomaterials or covalent modifications exist some shortcomings. For example, the undesirable conductivity and the low facilitation efficiency of MOF or COF nanomaterials might restrain the ECL launching efficiency [12]. The covalent modifications method still has a restriction in trace analysis as qualitative amplification [13].

Framework materials including COFs and MOFs are a novel category of porous materials linked by the covalent and coordination bonds with high porosity, large surface area and functional nature [14–16]. Theses merits endow framework materials with an admirable carrier to incorporate conductive materials such as mesoporous silica nanoparticles (MSNs) [17], carbon nanotubes [18], and load luminophore such as Ru $(bpy)_3^{2+}$ and its analogues [19–21]. Nevertheless, some intrinsic deficiencies in either MOFs or COFs restricted their further utilization in various fields. For instance, the pristine COFs manifest admirable chemical stability due to its covalent structure properties but possess weak crystallinity [22]. On the contrary, the pristine MOFs manifest laudable crystallinity but their chemical stability is limited [23]. Hence, exporing a new method to hybridize COFs and MOFs and make it possible for the obtained new hybrids (COF@MOF or MOF@COF) contains the beneficial characteristics of each component has become an urgent task to be solved.

Recent studies revealed that $Ru(bpy)_3^{2+}$/2-(dibutylamino)-ethanol (DBAE) system exhibits a much robust ECL efficiency in comparison with $Ru(bpy)_3^{2+}$/TPrA system due to the low toxicity, good stability and versatility of DBAE in contrast to TPrA [24,25]. Nonetheless, both as amine coreactants, DBAE has a similar reaction mechanism as TPrA [26]. It has been reported that the generation, transfer rate, and lifespan of $TPrA^{\bullet}$ are key decisive factors to affect ECL response [27]. DBAE has a similar luminescence mechanism to TPrA, but its co-reaction is better. However, the extra added DBAE floats on the surface of phosphate buffer solution (PBS) owing to its low solubility and the unstable transition state severely confined the survival of intermediate radicals.

The confinement-enhanced ECL technique entails the embedding of luminophor into confinement-enhancing materials, which constrains the free diffusion of luminophore molecules, amplifies their concentration, and improves the signal [28,29]. The technique of confinement-enhancement shows potential in resolving the various deficiencies in electron transfer between luminophores and co-reactants, leading to a substantial improvement in reaction efficiency. However, the reports on confinement-enhanced electrochemiluminescence in the field of electrochemiluminescence are currently few.

The γ-CD-MOF is a biocompatible porous framework material that consist of nontoxic K^+ ions and edible γ-cyclodextrin [30]. These favorable compositions endow γ-CD-MOF with admirble encapsulation capabilities. Previous studies have reported that COF-LZU1 possesses confined pore space and defined pore environment, which make it a promising material for sensor construction. For example, Zeng's group reported $Ru(bpy)_3^{2+}$ immobilized on imine-modified COF-LZU1 (Ru@COF-LZU1) for the detection of AFM1 [31]. Zhang's group used COF-LZU1@PEI@Fe_3O_4 as a m-*m*-dSPE adsorbent for the extraction of TCs [32]. Qiu's group used COF-LZU1 as a base material to adsorb the CA125 primary antibodies (Ab_1) [33]. Inspired by above-mentioned studies, considered the merits of γ-CD-MOF and unique characteristic of COF-LZU1, it can be envisioned that the hybridization of COF-LZU1 and γ-CD-MOF will fabricate new hybrids that possess the characteristics of each component due to the synergistic effects.

Noble metal aerogels (NMAs) are affiliated to a member of self-assembled porous nanostructures with large specific surface areas (SSAs), electrical conductivity and ample interconnected pores, which have sparked extensive explore in the field of biosensing [34]. As a typical 2D nanomaterial, molybdenum disulfide (MoS_2) is owned by the family of transition metal dichalcogenides (TMDs) with distinctive layered structure and high specific capacity [35]. The morphology of MoS_2 is presented different nanostructures such as nanosphere, nanoflower, nanosheet, and the nanostructures can be flexibly adjusted [36]. MoS_2 nanoflowers (MoS_2 NFs) have been provided large surface area and available reaction sites, which exhibit superb promise in various biosensors due to its brilliant conductivity and exceptional catalytic activity [37]. Combining the merits of MoS_2 NFs and NMAs, MoS_2 NFs were used as a substrate to grow Au–Pd–Pt NMAs on its surface with the induction of NH_4F. The gained Au–Pd–Pt NMAs@MoS_2 NFs possessed high-performance including large SSAs, high porosity and excellent electrical conductivity, which could facilitate the electron transport. The more available reaction sites can capture more Ab_1 by the interaction between amino and Au–Pd–Pt NMAs growing on the surface of MoS_2 NFs.

In this work, Au NPs decorated Ru@γ-CD-MOF@COF-LZU1 microreactors as signal label to capture detection secondary antibody (Ab_2) and Au–Pd–Pt NMAs@MoS_2 NFs as base material to capture Ab_1. The COF-LZU1 was applied as a coating on the exterior of γ-CD-MOF to obtain γ-CD-MOF@COF-LZU1. The newly formed hybrid porous material as confinement-enhancing material can encapsulate numerous Ru $(dcbpy)_3^{2+}$ and DBAE, improving the signal strength and promoting the redox processes by concentrating DBAE. In this work, COF-LZU1 acted as micro-reactors possessed many micro-reaction chambers can provide a mild environment to enhance the generation rate of $DBAE^{\bullet+}$ and the survival of $DBAE^{\bullet}$. Scheme 1 displayed the underlying mechanisms of Ru@COF-LZU1@γ-CD-MOF-Au. As expected, the sensor based on MOF@COF composites and Au–Pd–Pt NMAs@MoS_2 NFs was engineered and offered a new route to construct a novel ECL platform with excellent performance for CYFRA 21-1 detection.

2. Experimental section

2.1. Preparation of COF-LZU1@γ-CD-MOF composites

The γ-CD-MOF@COF-LZU1 composites were prepared by modifying a layer of COF-LZU1 on the exterior of γ-CD-MOF, using a previously reported method with a considerable rectification. The elaborated synthesis procedure of γ-CD-MOF was revealed in the Supporting Information (SI). Firstly, 120 mg of γ-CD-MOF and 32 mg of 1,3,5-benzenetricarboxaldehyde were dissolved in 8 mL of 1,4-dioxane solution and kept stirring for 15 min. The obtained solution was heated at 80 °C for 3 h in oil bath with forcefully stirring. Meantime, acetic acid (3 M, 1 mL) and 4 mL of 1,4-dioxane solution containing 32 mg *p*-phenylenediamine were added into the above solution orderly and kept stirring for 1 h. After that, the prepared suspension was degassed by argon and the mixture was placed into a Teflon-lined autoclave at 110 °C for 20 h. The obtained light-yellow powder was collected by centrifugation, followed by washing with tetrahydrofuran and acetone for 3 times respectively. The acquired COF-LZU1@γ-CD-MOF subjected to overnight drying and stored at ambient temperature for later using.

2.2. Preparation of Ru@COF-LZU1@γ-CD-MOF-Au composites

The Au NPs were synthesized on the surface of COF-LZU1@γ-CD-MOF by in-situ reduction method. First, 5 mL of COF-LZU1@γ-CD-MOF composites got ready. Next, 600 μL of trisodium citrate (400 mM) and 0.5 mL of $HAuCl_4$ (1%, w/v) aqueous solution were trickled into above solution with slowly stirring. After 30 min, 300 μL of sodium

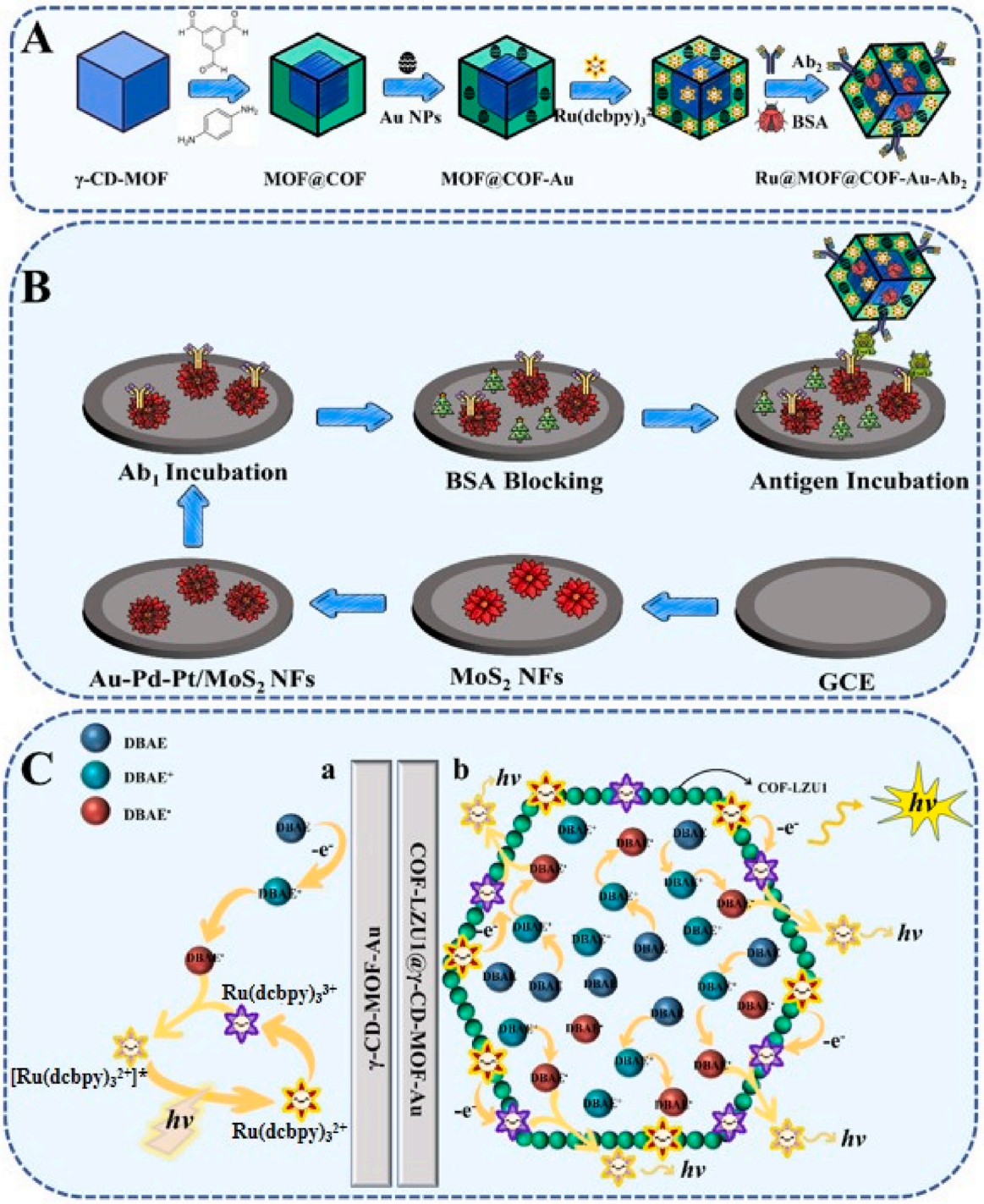

Scheme 1. (A) The preparation process of Ru@COF-LZU1@γ-CD-MOF-Au. (B) The illustrated fabrication diagram of the ECL immunosensor. (C) The ECL mechanism without (a) and with (b) COF-LZU1 micro-reaction chambers.

borohydride blend (0.2 M) was added dropwise into the suspension to reduce Au NPs on its surface of COF-LZU1@γ-CD-MOF and kept stirring for another 30 min. The gained COF-LZU1@γ-CD-MOF-Au composites were dried and collected after washing with ultrapure water and centrifugation. To prepare the Ru@COF-LZU1@γ-CD-MOF-Au composites, 1 mL of $Ru(dcbpy)_3^{2+}$ (0.5 mM) and 5 mg of as-prepared COF-LZU1@γ-CD-MOF-Au composites were blended together and shocked for 12 h. The gained suspension was maintained at 4 °C until the assembly of the sensor.

2.3. Preparation of Ru@COF-LZU1@γ-CD-MOF-Au-Ab_2 bioconjugates

The carboxyl group of $Ru(dcbpy)_3^{2+}$ was activated using biological coupling agents of 1-(3-(dimethylamino)propyl)-3-ethyl carbodiimide hydrochloride (EDC) and N-hydroxysuccinimide (NHS). Firstly, 1.0 mL of as-prepared Ru@COF-LZU1@γ-CD-MOF-Au dispersion solution (5 mg/mL) was mixed with 100 μL of EDC (400 mM), 100 μL of NHS (100 mM) and Ab_2 (100 μL, 10 μg/mL). At the same time, 400 μL of BSA solution (0.1%) was added to above that to block nonspecific binding sites. Afterwards, the mixture was shaken for 24 h at 4 °C. After

centrifugation, the gained Ru@COF-LZU1@γ-CD-MOF-Au-Ab_2 biomolecule conjugates were kept at 4 °C.

2.4. Preparation of MoS_2 NFs

The flower-like MoS_2 were synthesized by a beforehand method [38]. Hydrothermal method was used to synthesis MoS_2 NFs. Firstly, 1 g of $Na_2MoO_4{\cdot}2H_2O$ and 1.4 g of CH_4N_2S were intermixed together and solubilized into 100 mL of ultrapure water and agitate for 30 min until completely dissipated. Whereafter, 500 mg of C_6H_8O was been adding to the foregoing blend and stirring for 20 min to tune the pH value. The gained uniform solution was diverted into a Teflon-lined autoclave with a volume of 100 mL and kept warm at 210 °C for 21 h. The black powders were collected by centrifugation after washing with ultrapure water and ethanol. After drying overnight at 60 °C, the acquired powders were heat-treated at 800 °C for 1 h in an Ar atmosphere to increase their crystallinity.

2.5. Preparation of Au–Pd–Pt NMAs@MoS_2 NFs

NH_4F served as the starting agent to induce metal precursor forming metal aerogels for its brilliant salting-out capacity and great destabilization ability. Au–Pd–Pt NMAs were induced to grow on the surface of MoS_2 NFs by NH_4F. The detailed description was as follows: trisodium citrate (400 mM, 100 μL), K_2PtCl_4 (32.5 mM, 61.6 μL), $HAuCl_4$ (32.5 mM, 41.2 μL) and Na_2PdCl_4 (32.5 mM, 61.6 μL), MoS_2 solution (4 mg/mL, 500 μL) were added into 5 mL ultrapure water with sustained stirring for 30 min. After that, $NaBH_4$ (200 mM, 80 μL) were successively added dropwise into above solution. The solution turned black immediately implied the formation of nanostructured metal polymers. Then, NH_4F (1 mM, 2.22 mL) were continuously added dropwise in as-prepared Au–Pd–Pt NMAs@MoS_2 NFs solution to form Au–Pd–Pt NMAs@MoS_2 NFs after grounding for 6 h. The gained Au–Pd–Pt NMAs@MoS_2 NFs were gathered by centrifugation and resuspended in 2 mL ultrapure water and stored at 4 °C.

2.6. Preparation of Ab_1@Au–Pd–Pt NMAs@MoS_2 NFs

To prepare Ab_1@Au–Pd–Pt NMAs@MoS_2 NFs, 1 mg/mL of Au–Pd–Pt NMAs@MoS_2 NFs and Ab_1 (500 μL, 10 μg/mL) were blending and agitated at 4 °C for an overnight period. After centrifugation, the Ab_1@Au–Pd–Pt NMAs@MoS_2 NFs were placed in a suspension of PBS (pH 7.8) and preserved at 4 °C.

3. Results and discussion

3.1. Characterization of as-synthesized nanomaterials

Scanning electron microscope (SEM) presented cubic blocks with well-defined morphologies and the size of 300 − 500 nm (Fig. 1A). The

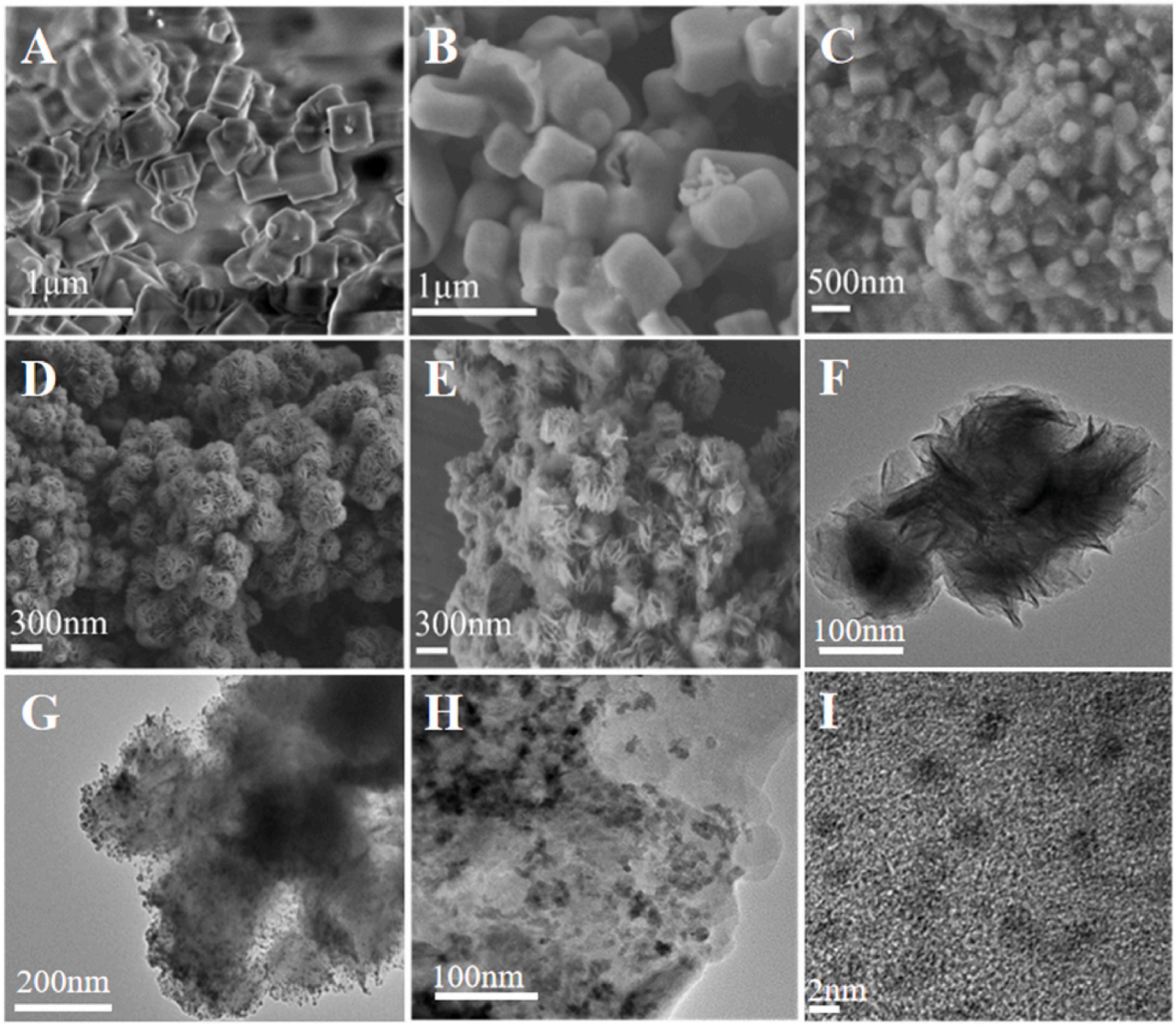

Fig. 1. SEM images of (A) γ-CD-MOF, (B) COF-LZU1@γ-CD-MOF, (C) Ru@COF-LZU1@γ-CD-MOF-Au composites, (D) MoS_2 NFs, and (E) Au–Pd–Pt NMAs@MoS_2 NFs. TEM images of (F) MoS_2 NFs, (G) & (H) Au–Pd–Pt NMAs@MoS_2 NFs. HRTEM image of Au–Pd–Pt NMAs (I).

structure and magnitude of COF-LZU1@γ-CD-MOF composites were comparable to that of γ-CD-MOF (Fig. 1B). With the COF-LZU1 modified on the surface of γ-CD-MOF, the cuboid morphologies were preserved and not distorted. The subtle change was that the outline of the cube became slightly blurred. Fig. 1C demonstrated the distribution of Ru@COF-LZU1@γ-CD-MOF-Au composites. The cubes entwined with each other and stacked together as $Ru(dcbpy)_3^{2+}$ combined with COF-LZU1@γ-CD-MOFs. Besides, elemental mapping analysis revealed the well distribution of Ru, Au, C and O in the Ru@COF-LZU1@γ-CD-MOF-Au composites (Fig. 2A), which indicated the successful doping of Ru and reduction of Au NPs.

X-Ray diffraction (XRD) was used to investigate the crystalline properties of prepared MoS_2 NFs (Figure. S1). The distinct peaks were scattered on 2θ at 14°(002), 33°(100), 39°(103), 49°(105), and 59° (110), matching the hexagonal crystal structure (JCPDS 37–1492). Transmission electron microscopy (TEM) and SEM were further characterized the morphology and structure of MoS_2 and corresponding composites. The flower-like nanospheres stacked up with a size of 400 — 700 nm (Fig. 1D). The single dispersed MoS_2 NFs manifested a petal size of 400 nm (Fig. 1F). Compared with pure MoS_2 NFs, it was noticeable that Au–Pd–Pt NMAs uniformly grew and distributed onto the surface of MoS_2 nano-petal (Fig. 1E). It was plain that fluffy gel grew on the edge of petal and intensively adhered to its surfaces (Fig. 1G and H). Fig. 1I depicted the HRTEM image of the Au–Pd–Pt NMAs, it can be observed that the well distribution of the gel in a uniform way. To further confirm the successful preparation of Au–Pd–Pt NMAs@MoS_2 NFs, the elemental composition analysis using X-ray photoelectron spectroscopy (XPS) was illustrated in Fig. 2B. The characteristic peaks of Au, Pt, Pd, Mo, S, C and O were existed in the synthetic composites, suggesting the successful synthesis of Au–Pd–Pt NMAs@MoS_2 NFs.

Besides, analyzing the pore properties of γ-CD-MOF and COF-LZU1@γ-CD-MOF through Brunauer-Emmett-Teller (BET) and Barett-Joyner-Halenda (BJH) evaluation. According to the isotherms of γ-CD-MOF and COF-LZU1@γ-CD-MOF, the corresponding pore size distribution shown in Figure S2, both of them exhibited a type I shape and existed micropores and mesoporous. The micropores of both materials were within 1 — 2 nm, and the mesopores were within 2 — 6 nm. As can be seen in Table S1, with COF-LZU1 modified on the surface of γ-CD-MOF, the newly synthesized composite material had a larger specific surface area and pore volume than the original γ-CD-MOF, and the average pore size is slightly reduced.

Inductively coupled plasma optical emission spectrometer (ICP-OES) as a sophisticated and precise methodology was employed with the intention of evaluating composite materials of Ru@COF-LZU1@γ-CD-MOF-Au's ability to encapsulate $Ru(dcbpy)_3^{2+}$ and the resulting encapsulation efficiency was determined. As specified in Table S2, the findings indicated that the calculated encapsulation ratio was approximately 70% with an encapsulated amount of 0.1749 μmol of $Ru(dcbpy)_3^{2+}$.

3.2. Electrochemical characterization of the biosensor

The layer-by-layer modification of different electrodes were detected and mutually corroborated the successful development of the immunosensor by cyclic voltammetry (CV) and electrochemical impedance spectroscopy (EIS). Stepwise modification curves are presented in Fig. 3A and B. As seen, bare electrode (curve a) manifested a reversible redox peak and corresponding a slight electron transfer resistance (Ret) was observed. With the modification of Au–Pd–Pt NMAs@MoS_2 NFs, a slightly greater resistance was gained. Despite the weak conductivity of MoS_2 (curve b), the electrode modified with Au–Pd–Pt NMAs@MoS_2 NFs still has a minor resistance due to the exceptional electron transfer ability of Au–Pd–Pt NMAs, the minor decline of the peak current reflected the inference. After the successive incubation with Ab_1, BSA and CYFRA 21-1, peak current (curves c, d and e) decreased furtherly, and the impedance sequentially increased. Finally, when the Ab_2@Ru@-COF-LZU1@γ-CD-MOF-Au bioconjugate (curve f) coated, this trend is being furtherly observed. All the above results showed the current response of CV data and impedance spectra of EIS were consistent with each other, indicating the triumphant assembly of the biosensor. The ECL performance of the different ECL probes is illustrated in Fig. 3C. The ECL response obtained for the Ab_1@Au–Pd–Pt NMAs@MoS_2 NFs-modified GCE (blue curve) is almost negligible, which can be attributed to the absence of ECL luminous material. When Ru@COF-LZU1@γ-CD-MOF-Au modified on the GCE (black curve), stronger ECL signal was obtained (black curves). This is attributed to the fact that γ-CD-MOF and COF-LUZ1 can encapsulate a large number of $Ru(dcbpy)_3^{2+}$ molecules and DBAE molecules, which greatly shortens the electron transfer path and improves the stability of the ECL signals. In addition, when Ab_2-Ru@COF-LZU1@γ-CD-MOF-Au was modified, the ECL signal was reduced (red curve), due to the fact that the non-conducting proteins

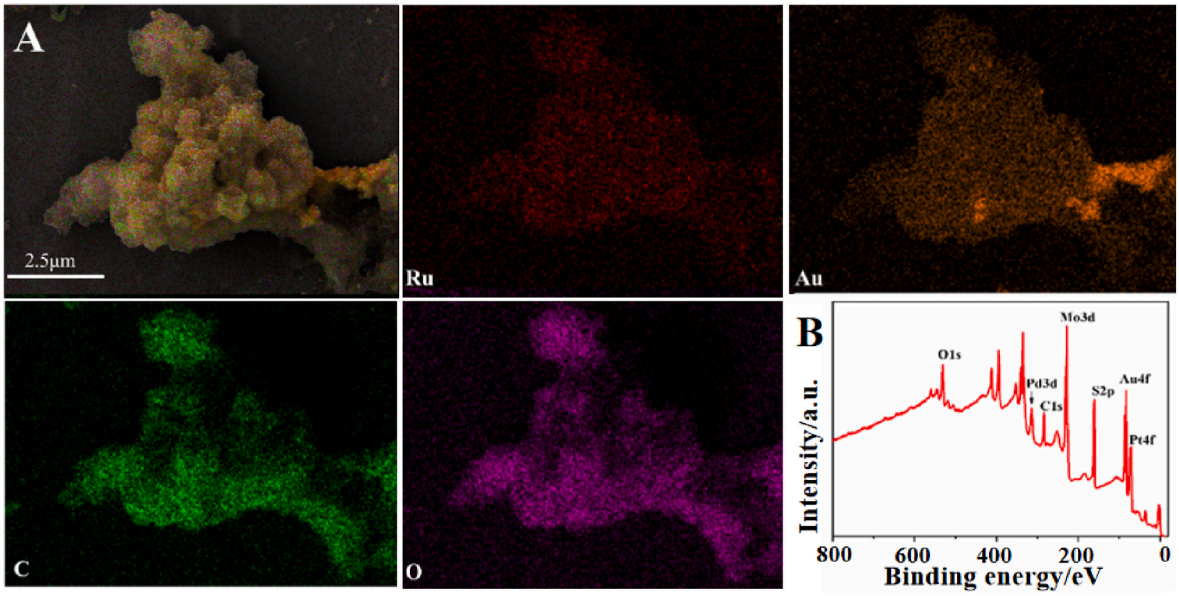

Fig. 2. Elemental mapping of Ru, Au, C, O elements corresponded to Ru@COF-LZU1@γ-CD-MOF-Au composites (A), respectively. XPS spectra for the whole region of Au–Pd–Pt NMAs@MoS_2 NFs (B).

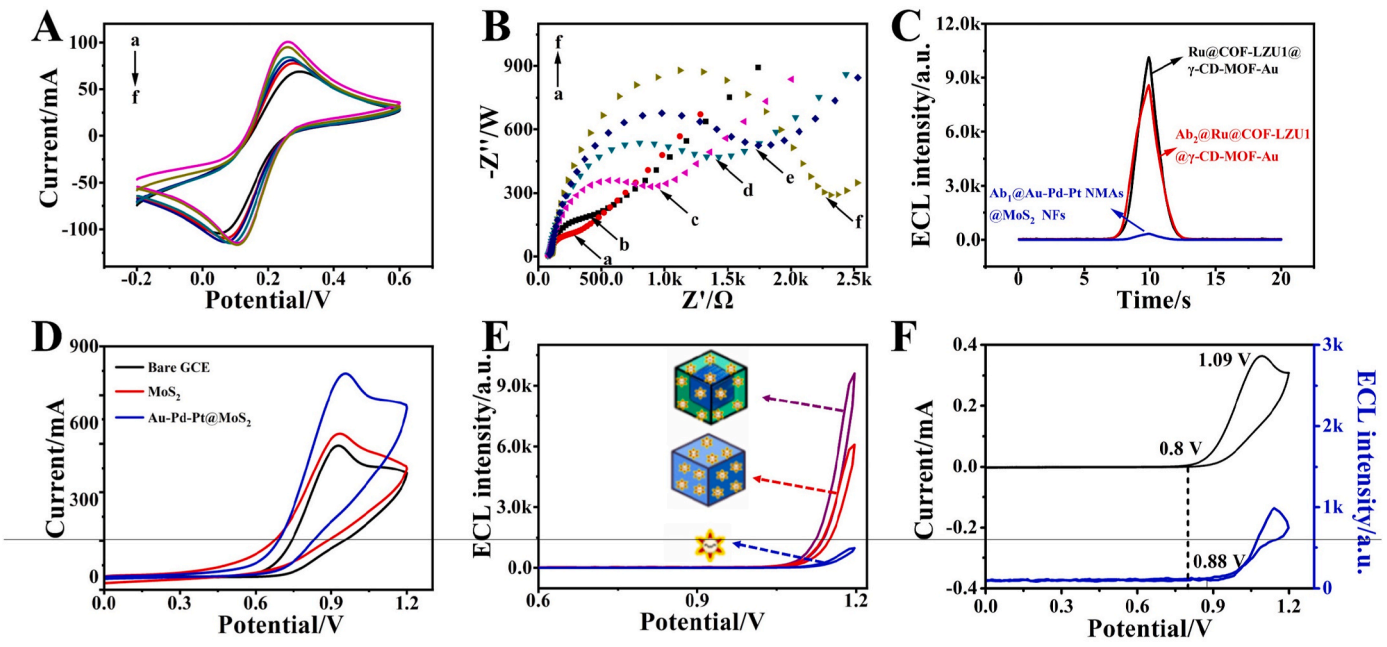

Fig. 3. CV curves (A) and EIS measurements (B) for: (a) bare GCE, (b) GCE/Au–Pd–Pt NMAs@MoS_2 NFs; (c) GCE/Au–Pd–Pt NMAs@MoS_2 NFs/Ab_1, (d) GCE/Au–Pd–Pt NMAs@MoS_2 NFs/Ab_1/BSA, (e) GCE/Au–Pd–Pt NMAs@MoS_2 NFs/Ab_1/BSA/CYFRA 21-1, (f) GCE/Au–Pd–Pt NMAs@MoS_2 NFs/Ab_1/BSA/CYFRA 21-1/Ab_2@Ru@COF-LZU1@γ-CD-MOF-Au; ECL curves (C) of Ru@COF-LZU1@γ-CD-MOF-Au (black curve), Ru@COF-LZU1@γ-CD-MOF-Au-Ab_2 (red curve), Ab_1@Au–Pd–Pt NMAs@MoS_2 NFs (blue curve); CV curves of Au–Pd–Pt NMAs@MoS_2 NFs/GCE, MoS_2 NFs/GCE and bare GCE tests in (D) 10 mL PBS containing DBAE (15 mM) and (E) ECL-Potential curves of pure $Ru(dcbpy)_3^{2+}$ (0.5 mM) in PBS (pH 7.8) without DBAE (blue curve), 5 mg/mL of Ru@γ-CD-MOF/GCE (red curve) and Ru@COF-LZU1@γ-CD-MOF/GCE (purple curve) in PBS (pH 7.8) with 50 mM DBAE; (F) ECL (blue curve) and CV (black curve) of the sensor.

inhibited electron transfer.

3.3. Electrochemistry studies of Au–Pd–Pt NMAs@MoS_2 NFs

Electrochemical processes of different modified electrodes were used for investigating the influence of substrate materials on DBAE and Ru $(dcbpy)_3^{2+}$ molecules. The oxidation behavior of DBAE was assayed in PBS electrolyte (Fig. 3D). Comparing with bare GCE and MoS_2-modified GCE in 15 mM of DBAE solution, Au–Pd–Pt@MoS_2-modified GCE presented a much more upgraded anodic current, denoting that Au–Pd–Pt@MoS_2 composites was capable of promoting the oxidation of DBAE in the PBS substrate. To further investigate the electrochemical oxidation process of Au–Pd–Pt NMAs@MoS_2 for $Ru(dcbpy)_3^{2+}$, the electrochemical oxidation process of GCE, MoS_2 modified electrodes and Au–Pd–Pt NMAs@MoS_2 modified electrodes was investigated. As can be seen from Figure S3, the Au–Pd–Pt NMAs@MoS_2 had the strongest oxidation current compared to the bare GCE, MoS_2 modified electrodes, suggesting that the modification also promoted the electrochemical oxidation process of $Ru(dcbpy)_3^{2+}$.

3.4. Confinement-enhanced ECL investigation of Ru@COF-LZU1@γ-CD-MOF/GCE

The success of confinement-enhanced effect can be exhibited by the disparity in ECL intensity observed in electrodes that are modified with different materials. Fig. 3E revealed that the ECL signal of the pure Ru $(dcbpy)_3^{2+}$ molecules were negligible when there was no coreactant present (blue curve). The addition of coreactant of DBAE led to a significantly stronger luminescence signal from Ru@COF-LZU1@γ-CD-MOF/GCE (purple curve) compared to Ru@γ-CD-MOF/GCE (red curve) at the same concentration. This suggested that the coreactant was essential for the ECL reaction and that modification with COF-LZU1 resulted in greater aggregation of DBAE molecules, thereby achieving confinement-enhancement.

3.5. Underlying mechanism of the ECL biosensor

The ECL intensity of $Ru(dcbpy)_3^{2+}$ was most frequently accompanied by the onset of oxidation of DBAE. As revealed in Fig. 3F, the injected DBAE presented a well-defined oxidation process with onset potential of +0.8 V and oxidation peak potential of +1.09 V (black curve). Concurrently, the ECL process was triggered at 0.9 V (blue curve), which corroborated the above statement. Negatively charged Au NPs can immobilise $Ru(dcbpy)_3^{2+}$ by electrostatic interaction, improving its stability and enhancing its ECL signal, improve the ECL luminescence efficiency [39]. Meanwhile, the loading of Au–Pd–Pt NMAs onto MoS_2 NFs not only improves the electron transfer capability, but also provides more active sites for the reaction of $Ru(dcbpy)_3^{2+}$ with DBAE [40]. COF-LZU1 used as a micro-reactor to provide improved $DBAE^{\bullet+}$ generation and $DBAE^{\bullet}$ survival rates, which promoting ECL response. Thus, the general luminous process of $Ru(dcbpy)_3^{2+}$-DBAE system could be adumbrated as eq (1)−4.

$$DBAE - e^- + Au - Pd - Pt \rightarrow DBAE^{\bullet+} \rightarrow H^+ + DBAE^{\bullet} + Au - Pd - Pt \quad (1)$$

$$Ru(dcbpy)_3^{2+} - e^- + Au - Pd - Pt \rightarrow Ru(dcbpy)_3^{3+} + Au - Pd - Pt \quad (2)$$

$$DBAE^{\bullet} + Ru(dcbpy)_3^{3+} \rightarrow [Ru(dcbpy)_3^{2+}]* \quad (3)$$

$$[Ru(dcbpy)_3^{2+}]* \rightarrow Ru(dcbpy)_3^{2+} + h\nu \quad (4)$$

It was worth noting that the electron generation and transfer rate of $DBAE^{\bullet+}$ and the survival of $DBAE^{\bullet}$ are the decisive factors to affect ECL emission. For this system, COF-LZU1 modified γ-CD-MOF made its surface possessed considerably more micro-reaction chambers. The tiny room can accommodate a certain amount of DBAE molecules due to its hydrophobic cavities, which boosted the oxidation efficiency of DBAE to generate more $DBAE^{\bullet+}$ and profited the survival of $DBAE^{\bullet}$.

3.6. Immunosensor optimization

The optimization conditions of the immunosensor can achieve the best performance [41–44]. Some key factors such as pH value of PBS (Fig. 4A) and concentration of DBAE (Fig. 4B) were evaluated. The pH maximum values hit at 7.8 of the PBS and 50 mM of the DBAE, which means that the antigen-antibody binding efficiency is maximized under these conditions. Thus, the most favorable values of pH and concentration of DBAE for the sensor were chosen at 7.8 and 50 mM respectively.

3.7. Analytical performance of the immunosensor

In contrast to pure $Ru(dcbpy)_3^{2+}$ (Fig. 4C), the continuously stable and gradually enhanced ECL signals (Fig. 4D) displayed the high stability of the immunosensor with the assistance of γ-CD-MOF and COF-LZU1, the former stabilized enormous $Ru(dcbpy)_3^{2+}$ molecules and the latter's micro-reaction chambers provided the benign reaction environment for $Ru(dcbpy)_3^{2+}$ and DBAE. Under optimized conditions, the ECL responses of Ru@COF-LZU1@γ-CD-MOF-Au-Ab_2 bioconjugates as probe at different concentrations of CYFRA 21-1 are displayed in Fig. 4E and F, the ECL signal increased with increasing CYFRA 21-1 concentration form 10 fg/mL to 50 ng/mL due to the fixation of $Ru(dcbpy)_3^{2+}$ molecules. The equation of the linear regression was $I = 1070.5 \lg c + 6469.7$ with a 0.99 correlation coefficient. Compared with other detection approaches of CYFRA 21-1 in Table S3, the lowest detectable concentration was 0.0055 pg/mL with a signal-to-noise ratio of 3 (S/N = 3). Above results showed the outstanding performance of the immunosensor and provided the possibility to the detection of CYFRA 21-1 in human serum.

3.8. Performance evaluation of the immunosensor

Some key factors to evaluate the immunosensor's performance were conducted. Selectivity of the immunosensor was assessed for detecting CYFRA 21-1, as illustrated in Fig. 5A. Common interferents in serum such as squamous cell carcinoma antigen (SCCA), carcinoembryonic antigen (CEA) and neuron-specific enolase (NSE) were used to comparatively detect. Compared with the mix samples (0.1 ng/mL of CYFRA 21-1) and pure CYFRA 21-1, the 100-fold concentration interfering substances (10 ng/mL) of SCCA, NSE CEA and blank control didn't generate a significant interference and exhibited near ECL intensities, which could be attributed to the specific recognition of antibody and antigen. Moreover, the repeatability of the immunosensor was investigated. Five parallel sets of electrodes were modified with 0.1 ng/mL of CYFRA 21-1 and the ECL intensities were almost constant with a relative standard deviation (RSD) of 0.44% (Fig. 5B). In addition, uninterrupted 600 s cyclic scans (Fig. 5C) that conducted in 10 mL PBS (pH 7.8) with 50 mM DBAE demonstrated the proposed immunosensor possessed admirable stability (RSD = 1.45%). Furthermore, the sensors were stored for 7 days at 4 °C. The ECL response of Fig. 5D shows good storage stability.

3.9. Serum sample analysis

The content of CYFRA 21-1 in human serum was extracted using the standard addition method to calculate the recoveries. Different concentrations of CYFRA 21-1 were diluted in human serum. 1.00, 3.00, 5.00 ng/mL were added to samples (Table S4), and the results revealed that the recoveries were between 99.0 and 102.7% with RSD between 2.8 and 3.9%, implying that the feasibility in serum sample detection.

4. Conclusion

A novel confinement-enhanced ECL immunosensor was constructed based on Ru@γ-CD-MOF@COF-LZU1-Au as micro-reactor and DBAE as coreactant for CYFRA 21-1 detection. The proposed immunosensor exhibited admirable chemical durability, satisfactory selectivity, and superb repeatability, which supported its feasibility in serum sample detection. This work offered a brand-new mean to fabricate highly efficient confinement-enhanced ECL immunosensor for other tumor marker detection in human serum.

CRediT authorship contribution statement

Xiang Ren: Writing – original draft, Data curation, Conceptualization. **Mingyue Shao:** Writing – review & editing, Methodology. **Xiaofei Li:** Writing – review & editing, Methodology. **Zuoxun Xie:**

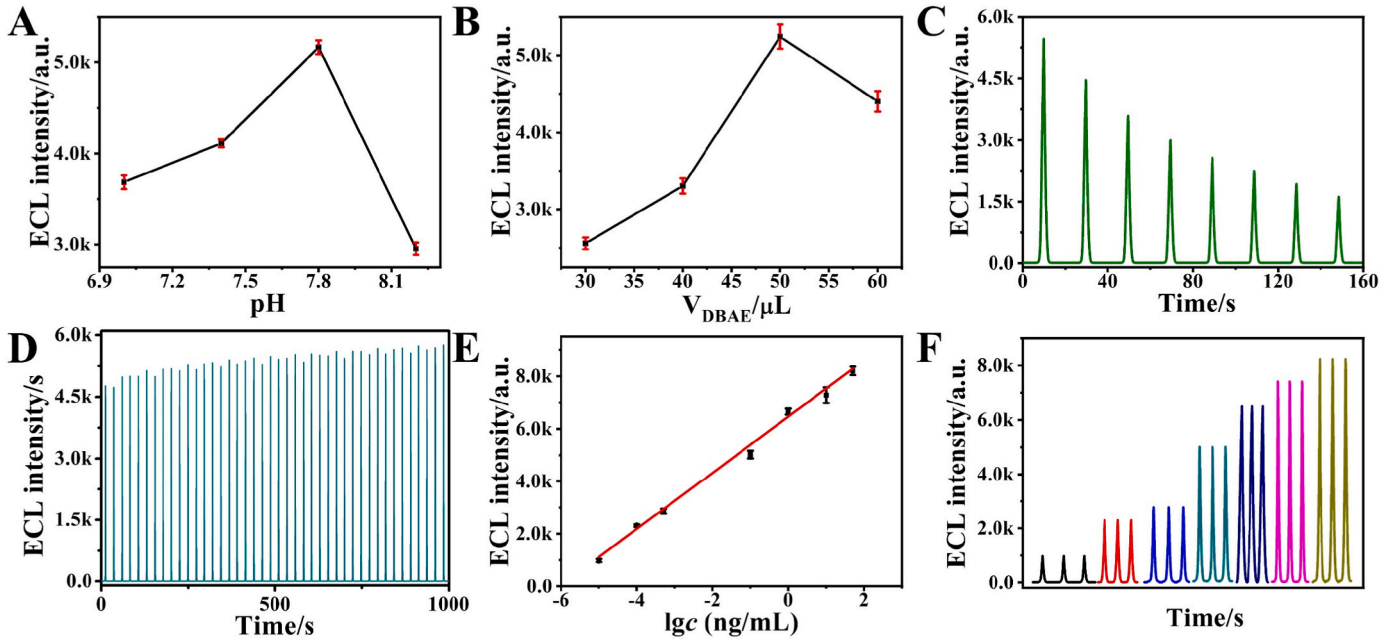

Fig. 4. Factors influencing the immunosensor: (A) pH and (B) DBAE concentration; ECL intensity-time curves of $Ru(dcbpy)_3^{2+}$ (C) and (D) the immunosensor when incubated with 0.1 ng/mL of CYFRA 21-1; calibration curve (E) and (F) the concentrations of CYFRA 21-1 form 10 fg/mL to 50 ng/mL.

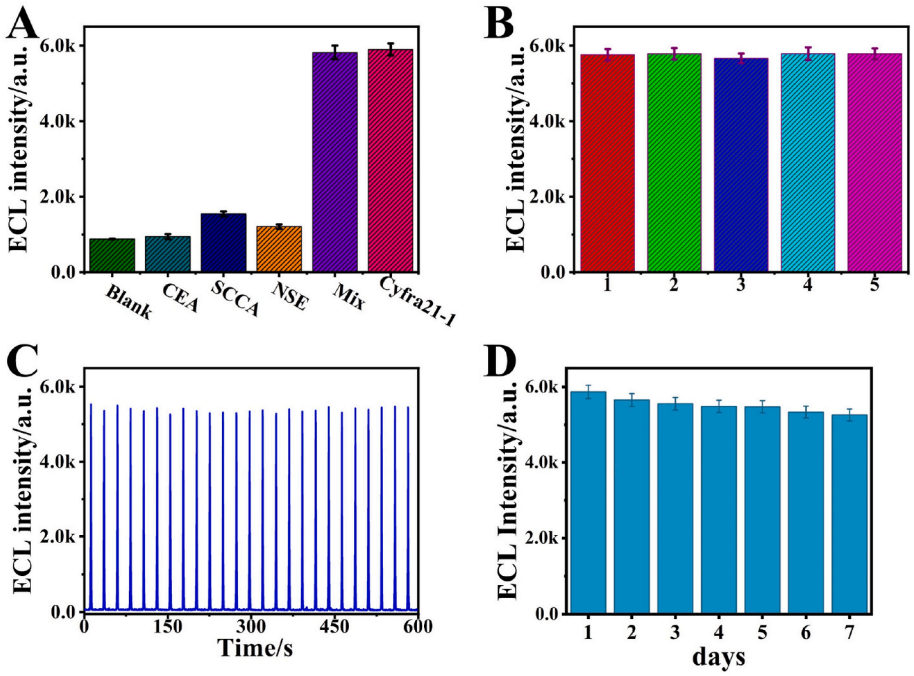

Fig. 5. (A) Influence of blank, 10 ng/mL of CYFRA 21-1, SCCA, NSE, CEA and mixture (10 ng/mL of SCCA, NSE, CEA + 0.1 ng/mL of CYFRA 21-1) on the ECL response; (B) repeatability of the immunosensor with 0.1 ng/mL of CYFRA 21-1 by five electrodes; (C) stability of the immunosensor with 0.1 ng/mL of CYFRA 21-1 under 600 s in 10 mL PBS (pH 7.8) with 50 mM of DBAE. (Error bars: SD, n = 5); (D) the storage stability of immunosensor over 7 days under a storage condition of 4 °C.

Methodology, Data curation. **Jinxiu Zhao:** Funding acquisition, Formal analysis. **Huan Wang:** Writing – review & editing. **Min Gao:** Methodology, Formal analysis. **Dan Wu:** Funding acquisition, Formal analysis. **Huangxian Ju:** Funding acquisition, Formal analysis. **Qin Wei:** Supervision, Project administration, Funding acquisition.

Declaration of competing interest

The authors declare that they have no known competing financial or personal relationships that could have appeared to influence the work reported in this paper.

Data availability

No data was used for the research described in the article.

Acknowledgements

This study was supported by the National Natural Science Foundation of China (No. 22204059, 22274062), the Natural Science Foundation of Shandong Province (No. ZR2021QB120), the Excellent Youth Innovation Team of Higher Education Institutions in Shandong Province (2023KJ317), the Yunnan Provincial Key Laboratory of Rural Energy Engineering (Yunnan Normal University) Open Fund (2022KF007).

Appendix A. Supplementary data

Supplementary data to this article can be found online at https://doi.org/10.1016/j.talanta.2024.125959.

References

[1] D. Calabria, E. Lazzarini, A. Pace, et al., Smartphone-based 3D-printed electrochemiluminescence enzyme biosensor for reagentless glucose quantification in real matrices, Biosens. Bioelectron. 227 (2023) 115146, https://doi.org/10.1016/j.bios.2023.115146.

[2] D. Wang, Y. Nie, Z. Li, et al., The controllable assembly of Cu nanocluster-based aggregation induced ECL strategy for miRNA detection, Anal. Chim. Acta 1238 (2023) 340607, https://doi.org/10.1016/j.aca.2022.340607.

[3] J. Zhao, J. Luo, D. Liu, et al., A coreactant-free electrochemiluminescence (ECL) biosensor based on in situ generating quencher for the ultrasensitive detection of microRNA, Sens. Actuators, B 316 (2020) 128139, https://doi.org/10.1016/j.snb.2020.128139.

[4] A. Zanut, F. Palomba, M. Rossi Scota, et al., Dye-Doped Silica nanoparticles for enhanced ECL-based immunoassay analytical performance, Angew. Chem., Int. Ed. 59 (49) (2020) 21858–21863, https://doi.org/10.1002/anie.202009544.

[5] Q. Zhao, J. Xue, X. Ren, et al., Competitive electrochemiluminescence aptasensor based on the Ru(II) derivative utilizing intramolecular ECL emission for E_2 detection, Sens. Actuators, B 348 (2021) 130717, https://doi.org/10.1016/j.snb.2021.130717.

[6] X.-L. Huo, Y. Chen, N. Bao, et al., Electrochemiluminescence integrated with paper chromatography for separation and detection of environmental hormones, Sens. Actuators, B 334 (2021) 129662, https://doi.org/10.1016/j.snb.2021.129662.

[7] S. Parajuli, X. Jing, W. Miao, Electrogenerated chemiluminescence (ECL) quenching of the $Ru(bpy)_3^{2+}$/TPrA system by the explosive TNT, Electrochim. Acta 180 (2015) 196–201, https://doi.org/10.1016/j.electacta.2015.08.107.

[8] X. Zhu, F. Kou, H. Xu, et al., A rapid and sensitive electrochemiluminescent sensor for nitrites based on C_3N_4 quantum dots on C_3N_4 nanosheets, RSC Adv. 6 (107) (2016) 105331–105337, https://doi.org/10.1039/C6RA22527F.

[9] S. Wang, C. Li, M. Saqib, et al., Quasi-photonic crystal light-scattering signal amplification of SiO_2-nanomembrane for ultrasensitive electrochemiluminescence detection of cardiac troponin I, Anal. Chem. 92 (1) (2020) 845–852, https://doi.org/10.1021/acs.analchem.9b03472.

[10] R. Luo, H. Lv, Q. Liao, et al., Intrareticular charge transfer regulated electrochemiluminescence of donor-acceptor covalent organic frameworks, Nat. Commun. 12 (1) (2021) 6808, https://doi.org/10.1038/s41467-021-27127-5.

[11] X. Qin, Z. Zhan, Z. Ding, Progress in electrochemiluminescence biosensors based on organic framework emitters, Curr. Opin. Electrochem. 39 (2023) 101283, https://doi.org/10.1016/j.coelec.2023.101283.

[12] J.-L. Zhang, Y. Yang, W.-B. Liang, et al., Highly stable covalent organic framework nanosheets as a new generation of electrochemiluminescence emitters for ultrasensitive microRNA detection, Anal. Chem. 93 (6) (2021) 3258–3265, https://doi.org/10.1021/acs.analchem.0c04931.

[13] F. Li, D. Wang, Q.-J. Xing, et al., Design and syntheses of MOF/COF hybrid materials via postsynthetic covalent modification: an efficient strategy to boost the visible-light-driven photocatalytic performance, Appl. Catal., B 243 (2019) 621–628, https://doi.org/10.1016/j.apcatb.2018.10.043.

[14] A. Kuc, M.A. Springer, K. Batra, et al., Proximity effect in crystalline framework materials: stacking-induced functionality in MOFs and COFs, Adv. Funct. Mater. 30 (41) (2020) 1908004, https://doi.org/10.1002/adfm.201908004.

[15] Z. Li, J. Guo, Y. Wan, et al., Combining metal-organic frameworks (MOFs) and covalent-organic frameworks (COFs): emerging opportunities for new materials

and applications, Nano Res. 15 (4) (2022) 3514–3532, https://doi.org/10.1007/s12274-021-3980-0.
[16] E. Ploetz, H. Engelke, U. Lächelt, et al., The chemistry of reticular framework nanoparticles: MOF, ZIF, and COF materials, Adv. Funct. Mater. 30 (41) (2020) 1909062, https://doi.org/10.1002/adfm.201909062.
[17] G. Zhan, H.C. Zeng, Integrated nanocatalysts with mesoporous silica/silicate and microporous MOF materials, Coord. Chem. Rev. 320−321 (2016) 181–192, https://doi.org/10.1016/j.ccr.2016.03.003.
[18] Y. An, S. Dong, H. Chen, et al., Ce-MOF/COF/carbon nanotube hybrid composite: construction of efficient electrochemical immune platform for amplifying detection performance of CA125, Bioelectrochemistry 147 (2022) 108201, https://doi.org/10.1016/j.bioelechem.2022.108201.
[19] C. Wang, N. Zhang, D. Wei, et al., Double electrochemiluminescence quenching effects of Fe_3O_4@PDA-CuXO towards self-enhanced $Ru(bpy)_3^{2+}$ functionalized MOFs with hollow structure and it application to procalcitonin immunosensing, Biosens. Bioelectron. 142 (2019) 111521, https://doi.org/10.1016/j.bios.2019.111521.
[20] Z. Wang, J. Yang, Y. Li, et al., Zr-Based MOFs integrated with a chromophoric ruthenium complex for specific and reversible Hg^{2+} sensing, Dalton Trans. 47 (16) (2018) 5570–5574, https://doi.org/10.1039/C8DT00569A.
[21] L. Zheng, Q. Guo, C. Yang, et al., Electrochemiluminescence and photoelectrochemistry dual-signal immunosensor based on $Ru(bpy)_3^{2+}$-functionalized MOF for prostate-specific antigen sensitive detection, SSens. Actuators, B 379 (2023) 133269, https://doi.org/10.1016/j.snb.2022.133269.
[22] T. Yang, Y. Chen, Y. Wang, et al., Weakly hydrophilic imine-linked covalent benzene–acetylene frameworks for photocatalytic H_2O_2 production in the two-phase system, ACS Appl. Mater. Interfaces 15 (6) (2023) 8066–8075, https://doi.org/10.1021/acsami.2c20506.
[23] K. Wang, H. Huang, X. Zhou, et al., Highly chemically stable MOFs with trifluoromethyl groups: effect of position of trifluoromethyl groups on chemical stability, Inorg. Chem. 58 (9) (2019) 5725–5732, https://doi.org/10.1021/acs.inorgchem.9b00088.
[24] G. Valenti, E. Rampazzo, S. Bonacchi, et al., Variable doping induces mechanism swapping in electrogenerated chemiluminescence of $Ru(bpy)_3^{2+}$ core-shell silica nanoparticles, J. Am. Chem. Soc. 138 (49) (2016) 15935–15942, https://doi.org/10.1021/jacs.6b08239.
[25] F. Yuan, K. Hao, S. Sheng, et al., 2-(Dibutylamino)ethyl acrylate as a highly efficient co-reactant of $Ru(bpy)_3^{2+}$ electrochemiluminescence for selective detection of cysteine, Electrochim. Acta 329 (2020) 135117, https://doi.org/10.1016/j.electacta.2019.135117.
[26] X. Li, X. Ren, L. Yang, et al., $Ru(dcbpy)_3^{2+}$-functionalized γ-cyclodextrin metal-organic frameworks as efficient electrochemiluminescence tags for the detection of CYFRA21-1 in human serum, Sens. Actuators, B 378 (2023) 133152, https://doi.org/10.1016/j.snb.2022.133152.
[27] H.-M. Wang, C.-C. Wang, A.-J. Wang, et al., Green synthesis of Pd nanocones as a novel and effective electrochemiluminescence illuminant for highly sensitive detection of dopamine, Sens. Actuators, B 281 (2019) 588–594, https://doi.org/10.1016/j.snb.2018.10.153.
[28] Y.-M. Lei, Y. Zhuo, M.-L. Guo, et al., Pore confinement-enhanced electrochemiluminescence on SnO_2 nanocrystal xerogel with NO_3^- as Co-reactant and its application in facile and sensitive bioanalysis, Anal. Chem. 92 (3) (2020) 2839–2846, https://doi.org/10.1021/acs.analchem.9b05367.
[29] J.-L. Zhang, S. Gao, Y. Yang, et al., Ruthenium(II) complex-grafted conductive metal-organic frameworks with conductivity- and confinement-enhanced electrochemiluminescence for ultrasensitive biosensing application, Biosens. Bioelectron. 227 (2023) 115157, https://doi.org/10.1016/j.bios.2023.115157.
[30] S.-T. Fan, Z.-J. Qiu, R.-Y. Xu, et al., Ultrahigh carbon dioxide-selective composite membrane containing a γ-CD-MOF layer, ACS Appl. Mater. Interfaces 13 (11) (2021) 13034–13043, https://doi.org/10.1021/acsami.0c18861.
[31] W.-J. Zeng, K. Wang, W.-B. Liang, et al., Covalent organic frameworks as micro-reactors: confinement-enhanced electrochemiluminescence, Chem. Sci. 11 (21) (2020) 5410–5414, https://doi.org/10.1039/D0SC01817A.
[32] Y. Zhang, Y. Ning, W. Liao, et al., Covalent organic framework-LZU1@PEI@Fe_3O_4-based magnetic dispersive micro-solid phase extraction of tetracyclines from environmental water prior to HPLC analysis, Anal. Methods 13 (37) (2021) 4320–4327, https://doi.org/10.1039/D1AY00873K.
[33] R. Qiu, W. Mu, C. Wu, et al., Sandwich-type immunosensor based on COF-LZU1 as the substrate platform and graphene framework supported nanosilver as probe for CA125 detection, J. Immunol. Methods 504 (2022) 113261, https://doi.org/10.1016/j.jim.2022.113261.
[34] H. Wang, Q. Fang, W. Gu, et al., Noble metal aerogels, ACS Appl. Mater. Interfaces 12 (47) (2020) 52234–52250, https://doi.org/10.1021/acsami.0c14007.
[35] M. Vizza, W. Giurlani, L. Cerri, et al., Electrodeposition of molybdenum disulfide (MoS_2) nanoparticles on monocrystalline silicon, Molecules 27 (17) (2022) 5416, https://doi.org/10.3390/molecules27175416.
[36] M. Salimi, M.A. Shokrgozar, D.H. Hamid, et al., Photothermal properties of two-dimensional molybdenum disulfide (MoS_2) with nanoflower and nanosheet morphology, Mater. Res. Bull. 152 (2022) 111837, https://doi.org/10.1016/j.materresbull.2022.111837.
[37] Y. Li, Q. Wang, H. Wang, et al., Novel Ag_2O nanoparticles modified MoS_2 nanoflowers for piezoelectric-assisted full solar spectrum photocatalysis, J. Colloid Interface Sci. 537 (2019) 206–214, https://doi.org/10.1016/j.jcis.2018.11.013.
[38] Y.-H. Tan, K. Yu, J.-Z. Li, et al., MoS_2@ZnO nano-heterojunctions with enhanced photocatalysis and field emission properties, J. Appl. Phys. 116 (6) (2014) 064305, https://doi.org/10.1063/1.4893020.
[39] B. Wang, X. Zhong, Y. Chai, et al., An ECL biosensor for sensitive detection of concanavalin a based on the ECL quenching of Ru complex by MoS_2 nanoflower, Sens. Actuators, B 245 (2017) 247–255, https://doi.org/10.1016/j.snb.2017.01.180.
[40] X. Ren, Z. Xie, H. Wang, et al., Ternary electrochemiluminescence quenching effects of $CuFe_2O_4$@PDA-MB towards self-enhanced $Ru(dcbpy)_3^{2+}$ functionalized 2D metal-organic layer and application in carcinoembryonic antigen immunosensing, Anal. Chim. Acta 1287 (2024) 342091, https://doi.org/10.1016/j.aca.2023.342091.
[41] Q. Zhao, Z. Gao, X. Liu, et al., Dual-signal integrated aptasensor for microcystin-LR detection via in situ generation of silver nanoclusters induced by circular DNA strand displacement reactions, Anal. Chem. 95 (38) (2023) 14317–14323, https://doi.org/10.1021/acs.analchem.3c02568.
[42] X. Dong, G. Zhao, Y. Li, et al., Dual-mechanism quenching of electrochemiluminescence immunosensor based on a novel ECL emitter polyoxomolybdate-zirconia for 17β-Estradiol detection, Anal. Chem. 94 (37) (2022) 12742–12749, https://doi.org/10.1021/acs.analchem.2c02350.
[43] Z. Xie, M. Shao, Z. Liu, et al., Ultrasensitive aggregation-induced electrochemiluminescence sensor for dopamine detection in polymer hydrogel system, Sens. Actuators, B 398 (2024) 134781, https://doi.org/10.1016/j.snb.2023.134781.
[44] D. Zhang, M. Gao, X. Xue, et al., Triple signal-enhanced electrochemiluminescence strategy using iron-based metal-organic frameworks modified with Ru(II) complexes for carcino-embryonic antigen detection, Talanta 267 (2024) 125239, https://doi.org/10.1016/j.talanta.2023.125239.